Biosensors and Bioelectronics 212 (2022) 114426

Contents lists available at ScienceDirect

Biosensors and Bioelectronics

journal homepage: www.elsevier.com/locate/bios

Performance of label-free optical biosensors: What is figure of merit (not) telling us?

Jiří Slabý, Jiří Homola *

Institute of Photonics and Electronics of the CAS, Chaberská 1014/57, 182 51, Prague, Czech Republic

ARTICLE INFO

Keywords:
Label-free biosensing
Optical biosensors
Plasmonics
Figure of merit
Refractive index resolution

ABSTRACT

Here we study the analytical performance of label-free optical biosensors with respect to analyte-induced refractive index changes that can be measured by a biosensor (refractive index resolution). We present an analytical model that interrelates the refractive index resolution and the parameters of the optical platform of a biosensor. We demonstrate that the figure of merit (FOM), which has been widely used to design optical platforms of label-free optical biosensors, is not an appropriate metric to guide the design or predict the performance of label-free optical biosensors. Therefore, we propose an extended definition of FOM that addresses its limitations. We confirm the validity of the proposed approach by both numerical simulations and experiments. Finally, we show that the analytical model of the refractive index resolution not only makes it possible to predict the performance of a biosensor but also provides strategies for achieving optimal performance.

1. Introduction

In the past three decades, label-free optical biosensors have advanced from a concept to a powerful technology with numerous applications in molecular biology and bioanalytics (Altug et al., 2022; Chen and Wang, 2020; Ligler and Gooding, 2019). A variety of label-free optical biosensors have been developed, including surface plasmon resonance biosensors (Estevez et al., 2014), biosensors based on whispering gallery modes (Vollmer and Arnold, 2008), biosensors employing modes of dielectric waveguides (Kozma et al., 2014) or ring resonators (Steglich et al., 2019). The label-free optical biosensors are complex devices that are comprised of multiple key elements (sensing structure, optoelectronic system, microfluidics, biorecognition elements, assay) and their analytical performance described by the limit of detection depends on a large number of factors. The contribution of an optical platform of a biosensor (sensing structure and optoelectronic system) is typically described by the refractive index resolution (the smallest measurable refractive index change), which can be correlated with the minimum detectable surface density of analyte molecules captured on the sensor surface (Altug et al., 2022). As optical label-free biosensors are basically refractometers that measure refractive index changes generated by the interaction between the analyte in a liquid environment and biorecognition element immobilized on the surface of a biosensor, initially, the main metric that was used to guide the design and optimization of label-free optical biosensors was the refractive index sensitivity. Later, when it was realized that the sensitivity alone is insufficient to predict or optimize the analytical performance of label-free optical biosensors, the figure of merit (FOM) was introduced. FOM is defined as a ratio between the sensitivity of the spectral feature associated with the excitation of an electromagnetic mode used for the sensing of refractive index and its spectral width (Hu et al., 2009; Priya et al., 2020; Sherry et al., 2006; van Gent et al., 1990); alternatively, in a few studies, FOM was expressed as a standard FOM multiplied with the depth of the spectral feature (Sinibaldi et al., 2012; Zhang et al., 2019). Due to its ease of use, FOM was quickly adopted and has become one of the main metrics used to assess and optimize the performance of optical platforms of label-free optical biosensors (especially with respect to the choice of materials and design of the sensing structure) (Dastmalchi et al., 2016; McPeak et al., 2015). Despite that, its link to the analytical performance of a biosensor has remained assumptive and has been rarely studied. One of the few exceptions was the study of the relationship between FOM and refractive index resolution in surface plasmon resonance (SPR) biosensors; however, the study was limited to sensors that used identical electromagnetic modes that were excited in the same geometry and with similar efficiency (Homola, 2006). Meanwhile, the need for the use of appropriate performance metrics and the standardization of the processes for their determination continued to be highlighted as an important challenge for the biosensor community

* Corresponding author.
E-mail address: homola@ufe.cz (J. Homola).

https://doi.org/10.1016/j.bios.2022.114426
Received 3 March 2022; Received in revised form 13 May 2022; Accepted 24 May 2022
Available online 27 May 2022

(Altug et al., 2022; Yang et al., 2020).

Herein, we show that, despite its vast popularity, FOM has a rather limited relationship to the analytical performance of label-free optical biosensors. In addition, we present theoretical analysis interrelating the FOM and the smallest analyte-induced refractive index changes that a biosensor can detect, and show how FOM could be modified to yield a more robust performance metric.

2. Theory

In order to explain the nature of FOM and its limitations, let us consider a biosensor based on a nanohole array as an example (Vala et al., 2019). Fig. 1 shows a typical reflectivity spectrum of the nanohole array calculated for the normal incidence using the finite-difference time-domain method. As follows from Fig. 1, the spectrum exhibits two resonance features (dips) that are associated with the excitation of two electromagnetic modes. The two modes exhibit spectral dips that have different widths and depths, and they also have different refractive index sensitivities (see caption of Fig. 1 for details). The figures of merit ($FOM = S/w$, where S is the sensitivity of the resonance wavelength to changes in the refractive index of the dielectric medium adjacent to the sensing structure and w is the width of the spectral dip) were calculated to be 61 RIU^{-1} and 3 RIU^{-1} for short- and long-wavelength resonances, respectively. In order to estimate the smallest analyte-induced refractive index change that the sensor can detect (refractive index resolution), we performed numerical simulations, in which we generated spectra with noise (corresponding to shot noise) and calculated the spectral positions of the features using the centroid method (Nenninger et al., 2002). The noisy spectra were generated by using random generator with Poisson distribution with a rate corresponding to the mean number of electrons expected in each pixel of the photodetector. The resulting sensor response-time series are shown in the inset of Fig. 1. Then, the refractive index resolution σ_{RI} was calculated from the sensor response series ($\sigma_{RI} = \sigma_{so}/S$ where σ_{so} is the standard deviation of the noise in the sensor output).

When we compare the performance of the two different modes of the nanohole array biosensor, we note that while the *FOM* for the short-wavelength mode is higher than that for the long-wavelength mode by a factor of 18, the refractive index resolution determined by the numerical simulations is better only by a factor of ~8. This is a rather large discrepancy (especially when considering that it involves two similar electromagnetic modes of one sensing structure) which indicates that the prediction of the refractive index resolution based on *FOM* is rather misleading. This is in large part because *FOM* only considers the properties of the electromagnetic modes and their excitation and neglects the properties of the optoelectronic system the sensing structure works in conjunction with.

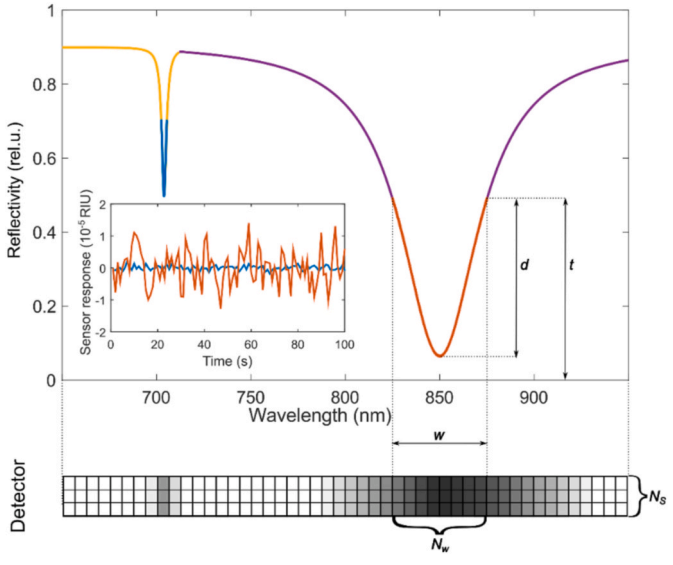

Fig. 1. Reflectivity spectrum for nanohole array (hole diameter – 200 nm, array period – 500 nm, gold layer thickness – 60 nm) with two different resonances at the wavelength of 703 nm (width – 3 nm, depth – 0.2, sensitivity – 183 nm/RIU) and 850 nm (width – 50 nm, depth – 0.425, sensitivity – 168 nm/RIU) projected on a 2D photodetector. N_T N_s = 100, N_w = 61 and N_w = 1001 for resonances at the wavelength of 703 and 850 nm, respectively. The inset shows the sensor response-time series for the two resonances.

Let us consider a biosensor based on the sensing structure that exhibits a spectral feature with a Lorentzian profile and on the optoelectronic system, the noise of which is dominated by shot noise of the light source (this is true for a majority of low-loss optical systems that employ standard light sources (Wang et al., 2011; Zhou et al., 2016)). The spectrum is described by means of a spectral series of light intensities (detected by individual pixels of a 2D photodetector, see Fig. 1) and the position of the spectral feature (i.e., sensor output) is determined by the centroid method (with the threshold set at 50% of the feature; the effect of the threshold on the sensor output is analyzed in (Nenninger et al., 2002)). We assume that the intensity spectrum is normalized in such a way that the normalized intensity equal to 1 produces the number of photoelectrons that fills the whole potential well of the photodetector.

In this study, we shall investigate the effect of noise in the light intensity series on the sensor output for two different scenarios. In the first scenario, we assume that the whole Lorentzian feature falls within the dynamic range of the photodetector (i.e., the normalized intensities assume values between $t - d \geq 0$ and $t + d \leq 1$, see Fig. 1). In experiments, such a situation is usually achieved by a proper choice of the intensity of illumination and integration time of the photodetector. We analyzed the propagation of noise through the centroid algorithm (details of the analysis are provided in Supplementary Material) and determined that the refractive index resolution can be expressed as follows:

$$\sigma_{RI} = \frac{1}{2\sqrt{N_T \cdot N_s \cdot N_w \cdot C}} \frac{\sqrt{t - 0.3d}}{d} \frac{w}{S} = A\left(\frac{\sqrt{t - 0.3d}}{d}\right) \frac{1}{FOM} = A\frac{1}{FOM^{+}}, \quad (1)$$

where N_T and N_s is the number of intensity values averaged timely and spatially, respectively, N_w is the number of points corresponding to the resonance feature width, C is the capacity of the photodetector (the number of electrons corresponding to the full capacity of the photodetector well), A is an optoelectronic constant $A = 1/(2\sqrt{N_T \cdot N_s \cdot N_w \cdot C})$, t is the threshold of the centroid method (only intensities below the threshold are considered in the centroid calculation), and d is the depth of the feature ($1 - d \geq t \geq d > 0$).

In the second scenario, we assume that the light levels can be increased in such a manner, that only a "useful" part of the Lorentzian spectral feature (i.e., the part that is used for centroid calculation) falls within the dynamic range of the photodetector. Then, the expression for the refractive index resolution (Eq. (1)) can be reduced to:

$$\sigma_{RI} = A\left(\sqrt{\frac{1}{d_{rel}}\left(\frac{1}{d_{rel}} - 0.3\right)}\right) \frac{1}{FOM} = A\frac{1}{FOM^{+}_{\mathrm{Imax}}}, \quad (2)$$

where $d_{rel} = d/t$.

3. Validation

The analytical model for the refractive index resolution was validated both numerically and experimentally. In the numerical simulation approach, we calculated the refractive index resolution using the simulated spectral features and computer-generated noise. Specifically, the spectra with shot noise were generated from the Poisson distributions with rates corresponding to the mean number of electrons

expected in each pixel of the photodetector when Lorentzian feature is recorded. The spectra were processed using the centroid algorithm to obtain the feature position and its variance. The following parameters were used in the numerical simulations: $N_w = 1001$, $C = 32700$, $N_t \cdot N_s = 100$, $S/w = 183/3\ \mathrm{RIU}^{-1}$; the total of 50 spectra were used to calculate the variance. In Fig. 2A and B, the results of numerical simulations are compared with those obtained from analytical models (Eqs. (1) and (2)) and show a very good agreement.

Experimental validation of the analytical model for the refractive index resolution was carried out using experimental spectra collected for spectral features with different characteristics. To generate spectral features with different characteristics, we used an SPR sensor based on the attenuated total reflection (Slabý et al., 2021) and SPR chips with different gold film thicknesses. The experimental parameters were: $N_T = 270, N_s = 20, C = 32700$; N_w was extracted for each feature independently. For each feature, the sensor response was recorded for 2 min (under the "constant" conditions) and the standard deviation of the sensor response (baseline noise) was calculated. Refractive index sensitivity was determined by measuring the sensor response for two solutions with different refractive indices (deionized water and 1 percent solution of NaCl in deionized water). Subsequently, the refractive index resolution was calculated for each feature using the sensitivity and baseline noise figures. Fig. 2C, which compares the refractive index resolutions predicted by the analytical model and those determined experimentally, suggests that the analytically predicted resolutions are in good agreement with the experimental values obtained for all the four considered features.

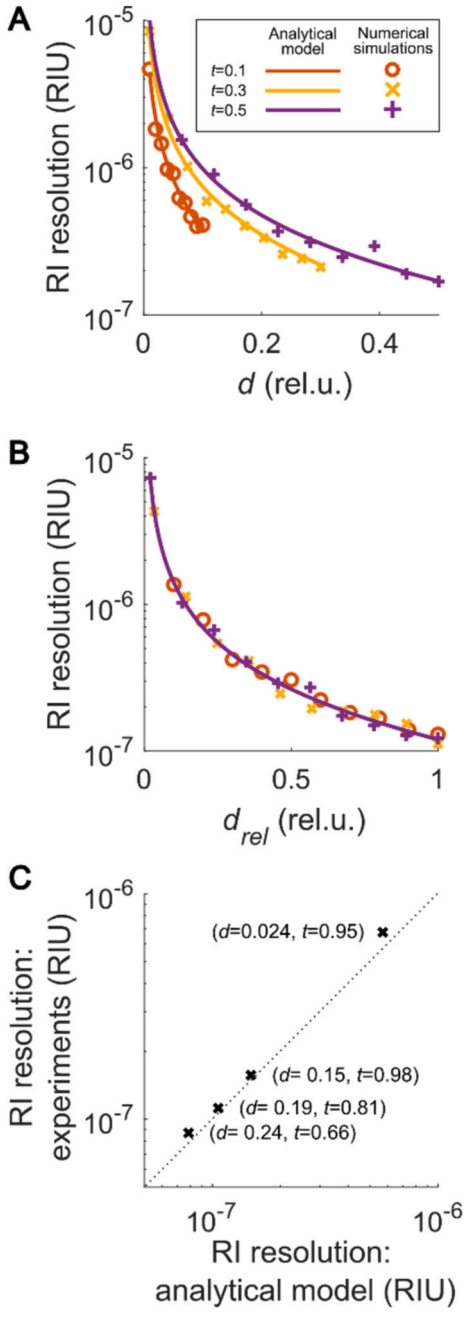

Fig. 2. Refractive index resolution as a function of feature depth calculated for three different threshold values using numerical simulations and: A) analytical model described by Eq. (1) and B) analytical model described by Eq. (2). C) Relationship between the refractive index resolutions determined by the analytical model and experiments for four different features (d and t values are given in the graph). The dotted line represents equal theoretical and experimental resolutions.

4. Results and discussion

As follows from the presented theory, the refractive index resolution can be expressed as a ratio of two terms: $\sigma_{RI} = A/FOM^{+}$. Whereas the first term (A) is associated solely with the optoelectronic system of a biosensor, the second term (FOM^{+}) is associated with the sensing structure and the coupling optics, which determine the characteristics of the resonance feature. It should be noted that the second term depends on the design of the biosensor and design parameters (e.g., material constants of the used materials).

While FOM^{+} is proportional to the traditional FOM, in contrast to FOM, FOM^{+} depends strongly on the depth of the resonance feature. Fig. 3 displays FOM^{+} as a function of d calculated for two different threshold values. Apparently, FOM^{+} increases nearly linearly with d, suggesting that the best refractive index resolution can be achieved when the resonance feature exhibits the maximum depth for a given threshold ($d = t$). The maximum value of FOM^{+} scales with $\sqrt{d}$ and reaches the highest value when the resonance feature fulfills: $d = t = 0.5$. When the sensor exploits the full dynamic range of the optoelectronic system (centroid threshold approaches the maximum intensity

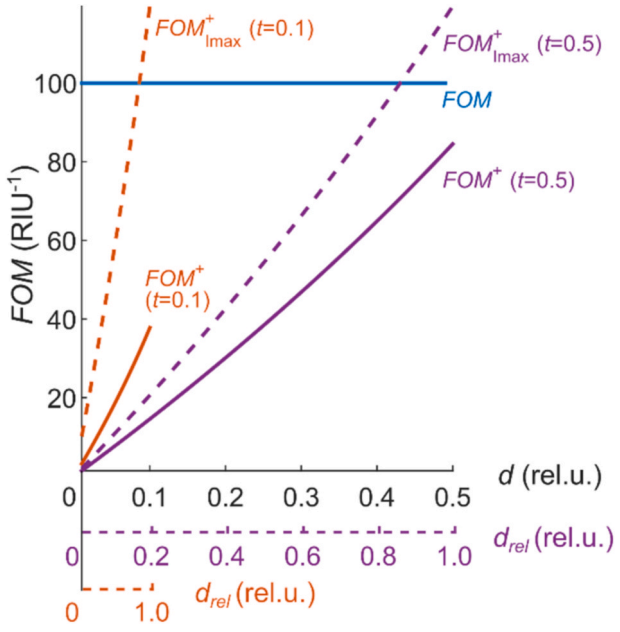

Fig. 3. FOM^{+} and FOM^{+}_{lmax} as a function of the depth of the resonance feature calculated for two threshold levels: $t = 0.1$ and 0.5. In simulations, it is assumed that $S/w = 100$. FOM is provided for comparison.

that can be measured by the photodetector), the second term equals to FOM^{+}_{Imax} (Eq. (2)). FOM^{+}_{Imax} increases nearly linearly with d_{rel} and reaches the highest value when $d_{rel}\rightarrow 1$ (corresponds to the situation that the resonance feature exhibits the maximum depth). Under such conditions, FOM^{+}_{Imax} is independent of the depth of the resonance feature and is equal to $1.2 \times FOM$. The following recommendations can be drawn based on the presented analysis – in order to achieve the best resolution: (1) sensing structures and the coupling optics should be employed that enable strong excitation of the electromagnetic modes leading to resonance features with the maximum depth and (2) maximum light levels in the optoelectronic system of a biosensor should be employed that bring the maximum intensity in the part of the resonance feature used for the calculation of the sensor output near the capacity of the photodetector. The latter shows that the sensing structures that exhibit weak spectral signals containing resonance features with high contrast are preferred over those that exhibit strong spectral signals containing rather shallow resonance features.

Factor A is related to the performance of a photodetector and is a function of two types of parameters. The first type ($N_T \cdot N_s \cdot N_w$) is related to the number of spectral intensities used for the calculation of the sensor output and their temporal and spatial averaging that reduces the noise of each intensity by a factor of $\sqrt{N}$, where $N = N_T \cdot N_s$ is the total number of averaged intensity values. The parameter of second type is the capacity of a photodetector (the number of electrons corresponding to the full capacity of the photodetector well). Factor A makes it possible to assess the potential of a photodetector for the construction of a high-performance biosensor and to compare photodetectors of different designs and operating spectral regions. Table 1 collects such parameters for the selected high-end photodetectors in the visible and near-infrared regions of the spectrum that were calculated assuming the sampling rate of 1 Hz (the time interval between the consecutive data points of the sensor response time series of 1 s). While the performance of the photodetectors expressed in terms of A varies within each considered spectral region, it appears that about the same performance can be offered by Si and InGaAs photodetectors in the visible and near-infrared spectral regions, respectively.

This comparison suggests that label-free optical affinity biosensors designed to operate in the visible and near-infrared spectral regions can achieve similar performance provided they exhibit similar FOM^{+} and the optoelectronic system of a biosensor employs a light source that can exploit the dynamic range of a photodetector to the same degree. While this may depend largely on the details of the used sensing structures and optoelectronic systems of the biosensor, in general, it may be more challenging to achieve this in NIR with commonly used low-cost light sources (e.g., halogen lamps); the availability of high performance yet cost-effective NIR photodetectors may be another concern. Regardless of the operating wavelength range, the presented analysis suggests that in order for the biosensor to achieve the best performance, it should employ a photodetector that offers a high frame rate, a high number of pixels that detect light associated with the resonance feature, and high photodetector well depth.

5. Conclusion

In this communication, we investigated the relationship between the analytical performance of a label-free biosensor (expressed in terms of the smallest analyte-induced refractive index changes that a biosensor can detect) and parameters of the biosensor's optical platform. We derived an analytical model of the refractive index resolution that interrelates the refractive index resolution with the characteristics of the resonance feature (both width and depth) and the parameters of an optoelectronic system of a biosensor (light levels and parameters of a photodetector). We also demonstrated that the conventional FOM is not an appropriate metric to guide the design of the optical platform of a biosensor and proposed an extended definition of FOM that addresses this deficiency as confirmed by both numerical simulations and experiments.

Table 1
Comparison of performance characteristics of selected 2D photodetectors in the visible and near-infrared regions of the spectrum.

Photodetector	Type	N_T	N_w	N_s	C	A ($\times 10^{-7}$)
Wavelength range: 400 – 1000 nm						
Basler ace acA1920-155um	CMOS	23	1920	1200	32700	1.4
Andor Zyla 5.5	CMOS	23	2560	2160	30000	1.2
Thorlabs Kiralux CS235MU	CMOS	23	1280	1024	10000	3.4
Thorlabs 1501M-USB	CCD	23	1392	1040	19500	6.2
Wavelength range: 700 – 1700 nm						
Sensors Unlimited 1280JSX	InGaAs	140	1280	100	1500000	1.0
Raptor Ninox 1280	InGaAs	60	1280	1024	450000	0.8
Princeton Instruments NIRwana HS	InGaAs	250	640	512	40000	2.8

CRediT authorship contribution statement

Jiří Slabý: Conceptualization, Methodology, Software, Writing – review & editing. **Jiří Homola:** Conceptualization, Funding acquisition, Supervision, Writing – review & editing.

Declaration of competing interest

The authors declare that they have no known competing financial interests or personal relationships that could have appeared to influence the work reported in this paper.

Acknowledgement

This research was supported by the Czech Science Foundation under contract 20–23787X.

Appendix A. Supplementary data

Supplementary data to this article can be found online at https://doi.org/10.1016/j.bios.2022.114426.

References

Altug, H., Oh, S.-H., Maier, S.A., Homola, J., 2022. Advances and applications of nanophotonic biosensors. Nat. Nanotechnol. 17 (1), 5–16.
Chen, C., Wang, J., 2020. Optical biosensors: an exhaustive and comprehensive review. Analyst 145 (5), 1605–1628.
Dastmalchi, B., Tassin, P., Koschny, T., Soukoulis, C.M., 2016. A new perspective on plasmonics: confinement and propagation length of surface plasmons for different materials and geometries. Adv. Opt. Mater. 4 (1), 177–184.
Estevez, M.C., Otte, M.A., Sepulveda, B., Lechuga, L.M., 2014. Trends and challenges of refractometric nanoplasmonic biosensors: a review. Anal. Chim. Acta 806, 55–73.
Homola, J., 2006. Surface Plasmon Resonance Based Sensors. Springer-Verlag Berlin Heidelberg.
Hu, J., Sun, X., Agarwal, A., Kimerling, L.C., 2009. Design guidelines for optical resonator biochemical sensors. JOSA B 26 (5), 1032–1041.
Kozma, P., Kehl, F., Ehrentreich-Förster, E., Stamm, C., Bier, F.F., 2014. Integrated planar optical waveguide interferometer biosensors: a comparative review. Biosens. Bioelectron. 58, 287–307.
Ligler, F.S., Gooding, J.J., 2019. Lighting up biosensors: now and the decade to come. Anal. Chem. 91 (14), 8732–8738.

McPeak, K.M., Jayanti, S.V., Kress, S.J., Meyer, S., Iotti, S., Rossinelli, A., Norris, D.J., 2015. Plasmonic films can easily be better: rules and recipes. ACS Photonics 2 (3), 326–333.
Nenninger, G.G., Piliarik, M., Homola, J., 2002. Data analysis for optical sensors based on spectroscopy of surface plasmons. Meas. Sci. Technol. 13 (12), 2038.
Priya, S., Laha, R., Dantham, V.R., 2020. Wavelength-dependent angular shift and figure of merit of silver-based surface plasmon resonance biosensor. Sensor Actuator Phys. 315, 112289.
Sherry, L.J., Jin, R., Mirkin, C.A., Schatz, G.C., Van Duyne, R.P., 2006. Localized surface plasmon resonance spectroscopy of single silver triangular nanoprisms. Nano Lett. 6 (9), 2060–2065.
Sinibaldi, A., Danz, N., Descrovi, E., Munzert, P., Schulz, U., Sonntag, F., Dominici, L., Michelotti, F., 2012. Direct comparison of the performance of Bloch surface wave and surface plasmon polariton sensors. Sensor. Actuator. B Chem. 174, 292–298.
Slabý, J., Bocková, M., Homola, J., 2021. Plasmonic biosensor based on a gold nanostripe array for detection of microRNA related to myelodysplastic syndromes. Sensor. Actuator. B Chem. 347, 130629.
Steglich, P., Hülsemann, M., Dietzel, B., Mai, A., 2019. Optical biosensors based on silicon-on-insulator ring resonators: a review. Molecules 24 (3), 519.
Vala, M., Ertsgaard, C.T., Wittenberg, N.J., Oh, S.-H., 2019. Plasmonic sensing on symmetric nanohole arrays supporting high-Q hybrid modes and reflection geometry. ACS Sens. 4 (12), 3265–3274.
van Gent, J., Lambeck, P.V., Kreuwel, H.J., Gerritsma, G.J., Sudhölter, E.J., Reinhoudt, D.N., Popma, T.J., 1990. Optimization of a chemooptical surface plasmon resonance based sensor. Appl. Opt. 29 (19), 2843–2849.
Vollmer, F., Arnold, S., 2008. Whispering-gallery-mode biosensing: label-free detection down to single molecules. Nat. Methods 5 (7), 591–596.
Wang, X., Jefferson, M., Hobbs, P.C.D., Risk, W.P., Feller, B.E., Miller, R.D., Knoesen, A., 2011. Shot-noise limited detection for surface plasmon sensing. Opt Express 19 (1), 107–117.
Yang, T., Chen, S., He, X., Guo, H., Sun, X., 2020. How to convincingly measure low concentration samples with optical label-free biosensors. Sensor. Actuator. B Chem. 306, 127568.
Zhang, R., Pu, S., Li, X., 2019. Gold-film-thickness dependent SPR refractive index and temperature sensing with hetero-core optical fiber structure. Sensors 19 (19), 4345.
Zhou, X., Zhang, L., Pang, W., 2016. Performance and noise analysis of optical microresonator-based biochemical sensors using intensity detection. Opt Express 24 (16), 18197–18208.